Title
The impact of residual solvent on catholyte performance in solid-state batteries

Journal
Journal of Materials Chemistry A, 10(47)

ISSN
2050-7488

Authors
Shen, Fengyu
Jonson, Robert A
Tucker, Michael C

Publication Date
2022-12-06

DOI
10.1039/d2ta04847g

Peer reviewed

The Impact of Residual Solvent on Catholyte Performance in Solid-State Batteries

Fengyu Shen[a]*, Robert A. Jonson[a], Michael C. Tucker[a]*

[a]Energy Storage and Distributed Resources Division, Lawrence Berkeley National Laboratory, Berkeley, CA 94720, United States

*: Author to whom correspondence should be addressed.

Email: fshen@lbl.gov (F. Shen) mctucker@lbl.gov (M.C. Tucker)

Abstract

All-solid-state batteries (ASSBs) are attractive due to their safety, use of Li metal anode, high energy density, and innovative processing routes. However, high interfacial resistance, especially on the cathode side, is one of the major challenges for commercialization of ASSBs. Catholyte, both liquid or solid, is added to lower the cathode/electrolyte interfacial resistance. In this study, we find that residual N-Methylpyrrolidone solvent remaining in a PVDF/LiTFSI solid polymer catholyte after incomplete drying can dramatically lower the interfacial resistance between $Li_{6.25}Al_{0.25}La_3Zr_2O_{12}$ electrolyte and $LiNi_{1/3}Mn_{1/3}Co_{1/3}O_2$ cathode active material. Cells with varying amounts of residual solvent are compared to optimize the residual solvent loading. With moderate residual solvent, the discharge capacity reaches 142 mA h/g when cycled at 25 °C and 0.5 C and the capacity retention is 60.5% after 125 cycles. Discharge capacity retention is improved at -10 °C. The conductivity of free-standing PVDF/LiTFSI

film, mimicking the PVDF/LiTFSI catholyte, verifies the role of residual NMP in the cathode. This study demonstrates the possibility of widely differing results for ASSBs when the cathode is not completely dried. Also, it provides a hint for a potential method to lower the cathode/electrolyte interfacial resistance.

Keyword: Solid-state battery, garnet, NMC cathode, residual solvent

1. Introduction

Lithium-ion batteries (LIBs) with high performance are widely used in portable devices and electric vehicles.[1, 2] With fast growth of the electric vehicle market, frequent fires and explosions for electric vehicles are focusing more attention on the safety of conventional LIBs which have flammable organic electrolyte.[3-5] All-solid-state batteries (ASSBs) using a solid-state electrolyte to replace the organic liquid electrolyte are regarded as the ultimate solution to improve the battery safety due to their nonflammable character.[6-8] Moreover, employing solid-state electrolytes can enhance the packing density of LIBs, thereby improving gravimetric and volumetric energy densities.[9] Garnet electrolytes show ionic conductivity greater than 1 mS cm^{-1} at room temperature,[10, 11] which is sufficiently high to support reasonable current densities in lithium-metal battery configurations. Also, they offer low electronic conductivity (~10^{-8} S cm^{-1} at room temperature) and wide electrochemical stability window (>6 V).[12, 13] Compared to other solid-state electrolytes with high ionic conductivities, such as sulfides, halides and LISICON, garnet electrolytes furthermore exhibit the best compatibility with Li metal anode.[14-17]

The high interfacial resistance between solid-state electrolytes and electrodes is one of the challenges for wide application of ASSBs. While there is extensive progress in integrating a Li metal anode with solid-state electrolytes,[18, 19] leading to extremely low interfacial resistance,[20, 21] there is less knowledge on integration of cathodes with solid-state electrolytes to obtain low interfacial resistance.[22-25] As a result, liquid catholyte is often relied on to reduce interfacial resistance in solid-state batteries (SSBs), which introduces safety and other concerns.[26-28] This work is motivated by the desire to produce a liquid-free ASSB, in this case with a composite catholyte of polyvinylidene fluoride (PVDF) and Lithium bis(trifluoromethylsulphonyl)imide (LiTFSI). While developing this cell design, we noticed that residual solvent remaining in the cathode after incomplete drying has a large impact on cell performance.

N-Methylpyrrolidone (NMP) is the most popular solvent for the electrode coating step in battery manufacturing as it readily dissolves PVDF which is the most common binder used in the battery industry. NMP has a high boiling temperature of 202 °C with a low vapor pressure of 3.413 mm Hg at 60 °C. With these properties, it is not easy to completely evaporate NMP from electrode tapes, and a standard drying procedure is not established. Various NMP drying protocols have been reported, and most cathodes were dried at or below 80 °C with or without vacuum assistance.[29-31] Moreover, the drying protocol is not even mentioned in some studies.[32, 33] NMP residue could therefore exist in some cathodes. It is known that appropriate solvent residue in solid-state electrolytes can enhance the ionic conductivity and stability with electrodes, resulting in a better electrochemical performance.[34-38] This even works for moisture remaining in the

components of conventional liquid batteries.[39] The impact of residual solvent on the performance of cathodes, however, is seldom discussed.

In this study, the impact of residual NMP is explored for cathodes with solid-state PVDF-LiTFSI catholyte, in contact with Al-doped garnet pellets. The loading of residual NMP solvent in a cathode containing $LiNi_{1/3}Mn_{1/3}Co_{1/3}O_2$ (NMC111) is evaluated for various drying protocols, and the LiTFSI content in the cathode is optimized. The durability of the cells at high (60 °C), moderate (25 °C), and low (-10 °C) temperatures is assessed. The performance of the cells with residual NMP is comparable to a hybrid cell with liquid electrolyte on the cathode side.

2. Experimental

2.1. Garnet electrolyte preparation

Commercial $Li_{6.25}Al_{0.25}La_3Zr_2O_{12}$ (LLZO) powder (Ampcera, USA) was used in this study.[40] As-received LLZO powder (0.5 g) was pressed at 400 MPa in a die with a diameter of 15 mm. Pellets were sintered at 1120 °C for 5 h in Ar atmosphere with heating and cooling rates of 2 °C min^{-1}. Graphite sheets were placed between the pellets and Al_2O_3 substrates during sintering to prevent reaction. The LLZO pellets were not buried in mother powder during sintering. Sintered pellets were ~0.7 mm thick and dry polished with 240, 400, 600, 800, 1200 grit SiC sandpapers sequentially. The thickness of the polished pellets is ~0.3 mm and the relatively density is ~94%.

2.2. Cell assembly

Au was sputter-coated on both sides for symmetric cells and only on the anode side for full cells, as Au coating can dramatically lower the interfacial resistance between Li metal and LLZO electrolyte.[41] The diameter of the gold coating is controlled by a mask with a diameter of 3/8 inch. A Li anode of the same size was punched from a Li foil (China Energy Lithium Co., Ltd., China) and melted on the Au coating at 220 °C on a hot plate in an Ar-filled glove box.

NMC111 slurry was mixed by roller milling NMC111 (MTI corporation, USA), carbon black (Alfa Aesar, USA), PVDF (Alfa Aesar, USA) and LiTFSI (Alfa Aesar, USA) in NMP (Alfa Aesar, USA) with zirconia milling balls. Carbon black and PVDF loadings are both fixed to be 15 wt.% of NMC111, and the amount of LiTFSI varies. The solid loading in the slurry is ~19 wt.%. A drop of this NMC111 slurry was directly spread on the uncoated face of the LLZO pellet electrolyte. The cathode area was kept similar to the Li metal anode. The cell was dried on a hot plate at 75 °C in an Ar-filled glove box. The active cathode loading is 1.5-2 mg cm^{-2}. All symmetric cells and full cells were assembled into coin cell holders.

2.3. PVDF/LiTFSI film

PVDF (0.25 g) and LiTFSI (0.2 g) were dissolved in NMP (2.25 g) and tape cast on a Mylar substrate in an Ar-filled glove box. The film was dried at 50 °C for 12 h and peeled off of the substrate. Several small free-standing films were removed with a ½ inch circle-punch for ionic conductivity measurement in the glove box. These films were further dried

at 75 °C in the glovebox for 20 h before ionic conductivity measurement. They were taken out of the glove box and exposed to air for 10 min before another ionic conductivity measurement.

2.4. Electrochemical measurement

Electrochemical impedance spectroscopy (EIS) was carried out using a VSP300 (BioLogic, France) potentiostat with a voltage amplitude of 10 mV in the frequency range from 7 MHz to 0.1 Hz. Au was sputter coated on both sides of LLZO electrolytes as an ion-blocking electrode for ionic conductivity measurement or as an interfacial layer for Li electrode melting. Full cells were cycled between 3 V and 4.3 V with various C rates (1 C=200 mA g^{-1}) in a thermal chamber (Model 107, TestEquity, USA) to control the temperature. The temperature control tolerance is ±0.5 °C. For free-standing PVDF/LiTFSI thin films, stainless steel was used as the ion-blocking electrode with gentle pressure provided by a clamp. Linear sweep voltammetry (LSV) was performed in a stainless steel/Li cell using a PVDF/LiTFSI film.

2.5. Characterization

The cross section and surface of samples were observed using a scanning electron microscope (SEM, JSM-7500F, JEOL, USA). Crystal structures were characterized by x-ray diffraction (XRD, D2 Phaser, Bruker, Germany), with 10° min^{-1} scanning speed at 0.02° step size. Pre-dried cathodes were heated to 100 °C and held for 4 h to qualitatively determine residual NMP loading with thermogravimetric analysis in Ar atmosphere (TGA,

TGA 4000, PerkinElmer, USA). Microtomography was conducted at the Advanced Light Source (ALS) Beamline 8.3.2 at Lawrence Berkeley National Laboratory, with pixel size of 0.65 μm. Images were collected over 180° in 0.072° steps, with 24 keV X-ray. The 3D reconstructions were performed with TomoPy, and visualization and image were analyzed with Avizo software.

3. Results and discussion

3.1 Garnet electrolyte characterization

Dense LLZO electrolytes with pure cubic phase were obtained through three steps of pressing, sintering and polishing. The XRD pattern of an as-sintered LLZO pellet shows severe Li-deficiency on the surface, Figure 1a. $La_2Zr_2O_7$ and La_2O_3 phases are detected, but these impurities are removed by polishing, resulting in pure cubic LLZO. This indicates that the thickness of the Li-deficient layer on the surface is less than 200 μm. SEM images show grain size of 2 to 4 μm before polishing and a smooth surface after polishing, Figure 1b and c. Such small grain size is beneficial for limiting dendrite growing.[42] A fresh fracture section surface reveals a dense structure with some small closed pores with pore size less than 5 μm, Figure 1d.

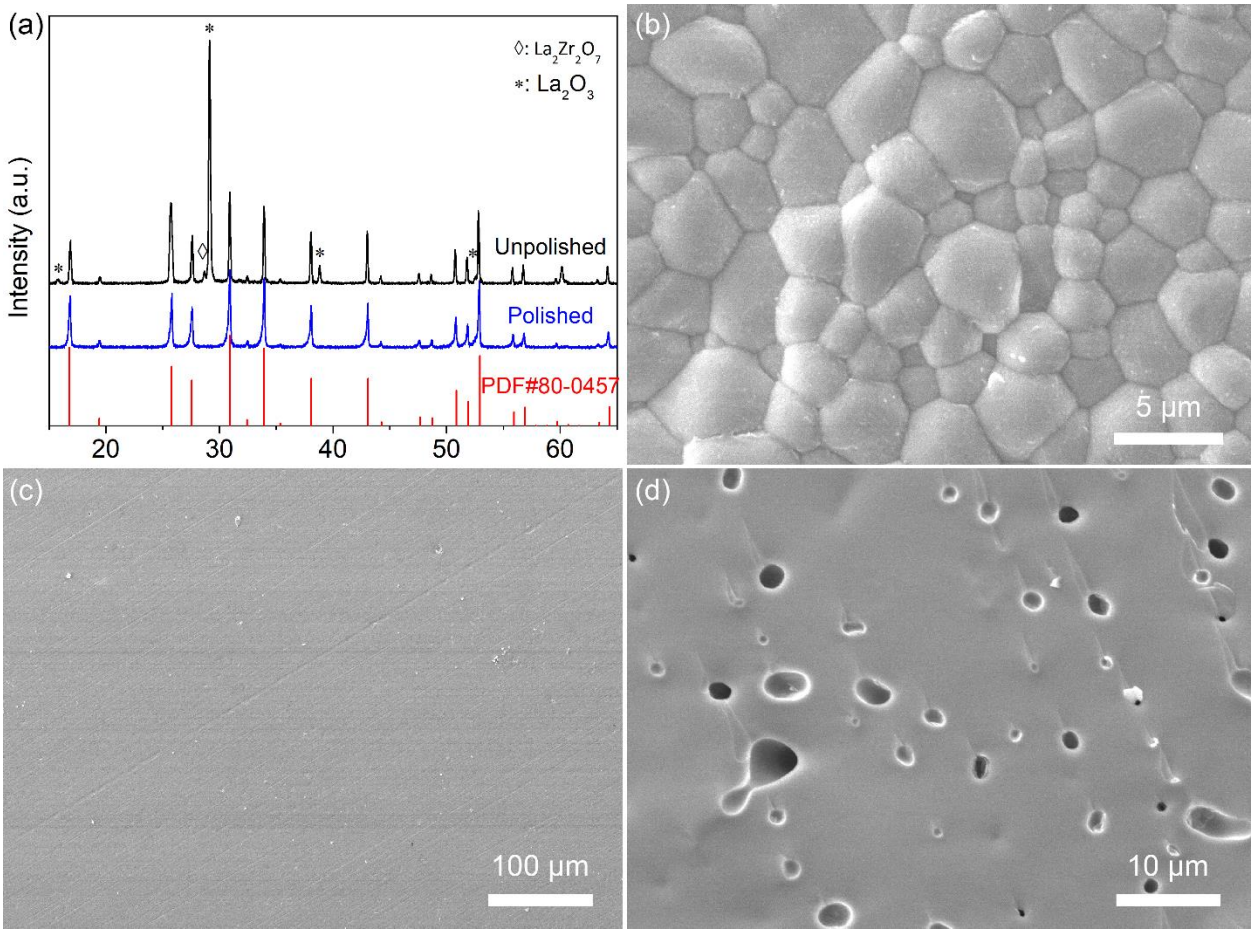

Figure 1. Phase analysis and microstructure of LLZO pellets. (a) XRD patterns of LLZO pellets as-sintered and after polishing; Microstructure of the surface (b) before and (c) after polishing, and (d) a fresh fracture section.

Ionic conductivity was determined at 25 °C by EIS with Au coating as the ion-blocking electrode. As is typical for LLZO electrolytes, two EIS semicircles are present at high frequency (>10 kHz) and are attributed to bulk and grain boundary conductivities respectively, Figure S1. The tail at the low frequency is ascribed to Li^+ blocking when Au electrodes are applied. The conductivity is calculated to be 3.4×10^{-4} S cm^{-1} at 25 °C. The

electrochemical performance of the electrolyte was established by galvanostatic cycling a Li/LLZO/Li symmetric cell, Figure 2. The cell was cycled at 0.2 mA cm^{-2} for 50 cycles, and 0.35 mA cm^{-2} for 100 cycles, followed by cycling to failure at 0.5 mA cm^{-2}. The period is 2 h for each full cycle. The overpotentials are stable for many cycles at ~43 mV and ~78 mV for 0.2 and 0.35 mA cm^{-2} current densities, respectively. This is consistent with the stability of the LLZO conduction and LLZO/Li interfacial resistances shown by EIS, Figure 2b. The symmetric cell is short-circuited after cycling at 0.5 mA cm^{-2} for 15 min due to dendrite growth, which is confirmed by EIS. Thus, the thin LLZO electrolyte (~0.3 mm) in this study can survive at 0.35 mA cm^{-2} for many cycles, which is ~25% higher than the current density corresponding to the 1 C rate for typical cathode loadings used in this study.

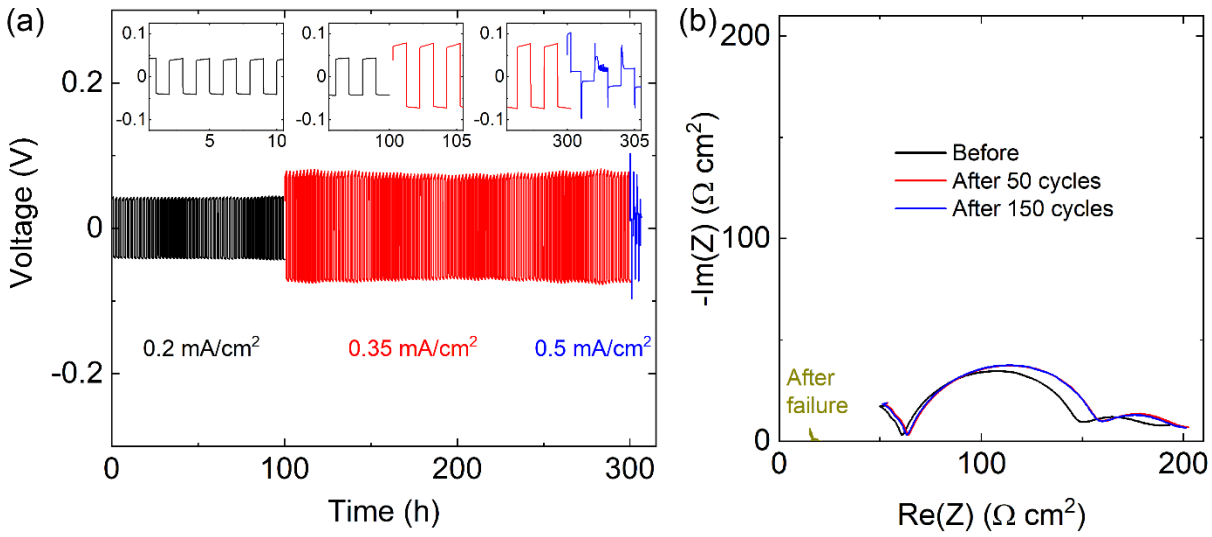

Figure 2. Symmetric cell performance. (a) Voltage profile for Li plating/stripping at 25 °C with current densities of 0.2, 0.35 and 0.5 A cm^{-2} and (b) corresponding EIS.

3.2 Cell processing and characterization with residual NMP

Residual NMP solvent in the cathode dramatically impacts the interfacial resistance and is also expected to swell the PVDF and reduce its mechanical properties, presenting a tradeoff. The amount of residual NMP was analyzed and optimized. In order to lower the interfacial resistance between LLZO and the cathode, cathode slurry was cast on LLZO directly.[22, 43] The slurry was then dried on a pre-heated hot plate at 75 °C. The slurry started drying from the edge to the center and it took ~7 min to eliminate all the visible liquid (Figure S2). Residual NMP solvent still remains in the cathode and was analyzed by TGA. The residual NMP content is 8.6% of the cathode weight when it was dried at 75 °C for 7 min, 3.3% for 15 min, and 1.8% for 30 min, with no detectable NMP remaining after overnight drying at 100 °C under vacuum, Figure S3. Cathodes with different drying times, and therefore different NMP contents, were compared in full cells, Figure 3a. The semicircles assigned to the LLZO conductivity at high frequency (~80 Ω cm^2) are consistent for the multiple cells, demonstrating repeatability of the LLZO electrolytes. The LLZO/cathode interface resistance is highly dependent on the drying time and the amount of residual NMP, as the semicircles at low frequency increase with drying time. The minimum total resistance is ~650 Ω cm^2, obtained when the cathode was dried for 7 min. Less drying of the cathode does not yield smaller interfacial resistance, presumably because PVDF remains dissolved in NMP, leading to weak bonding and no long-range polymer electrolyte conduction path. As a comparison, the resistance of a cell with no residual NMP (cathode dried overnight under vacuum at 100 °C) is extremely high (~$7x10^6$ Ω cm^2), Figure S4. The high interfacial resistance on the cathode side prevented cycling. The LiTFSI concentration in the cathode was also optimized, Figure 3b. The total

resistance is as small as 350 Ω cm^2 when the LiTFSI loading is 8.5% or more. Based on these observations, a cathode with 8.5% LiTFSI and dried at 75 °C for 7 min was selected for further studied below.

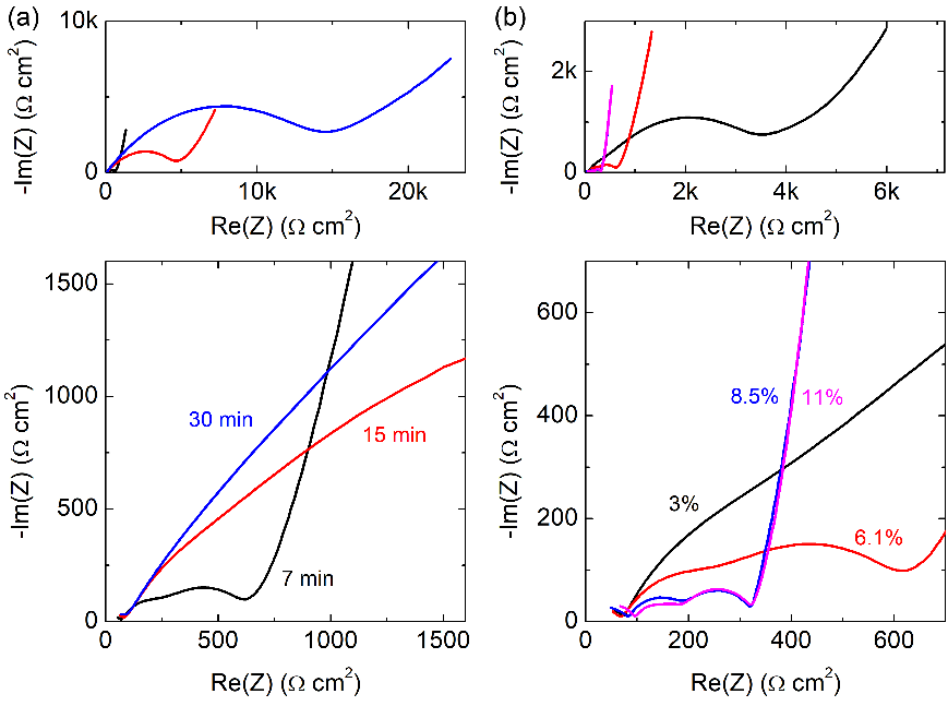

Figure 3. Optimization of NMP residue amount and Li salt loading. EIS of the full cells with different (a) cathode drying times with 6.1% LiTFSI and (b) Li salt loadings in the cathode dried at 75 °C for 7 min.

As the cathode is cast on LLZO electrolyte directly, the compatibility between the cathode slurry solution and LLZO must be evaluated. A polished electrolyte pellet was soaked in PVDF/LiTFSI/NMP solution for 20 h, followed by washing with NMP solvent. There are no visible color changes and the ionic conductivity is still the same as before soaking, Figure S5. This demonstrates that there is no degradation of the LLZO electrolyte when

contacting with cathode slurry directly. In particular, LLZO appears to be compatible with NMP, so we anticipate that the presence of residual NMP in the cathode will be acceptable.

The polished cross section of a fresh cell with NMP residue and mounted in epoxy to avoid delamination is shown in Figure 4. The Au coating enables Li metal to wet the LLZO without visible voids. The cathode also has a good contact with the electrolyte. The thickness of the cathode layer is 20 to 25 μm. The morphology of the cathode surface is shown in Figure 4e. The large agglomerates are NMC111 particles and the small particles are carbon black. A completely dried cathode with 8.5% LiTFSI was characterized by synchrotron X-ray spectroscopy and the 3D reconstruction image is shown in Figure S6. Only NMC111 is present in the image and the other components appear as voids based on their contrast difference. The NMC111 particles distribute uniformly in the cathode. The calculated volume of NMC111 through 3D-reconstruction is 47%, consistent with the cathode recipe (45 vol.%).

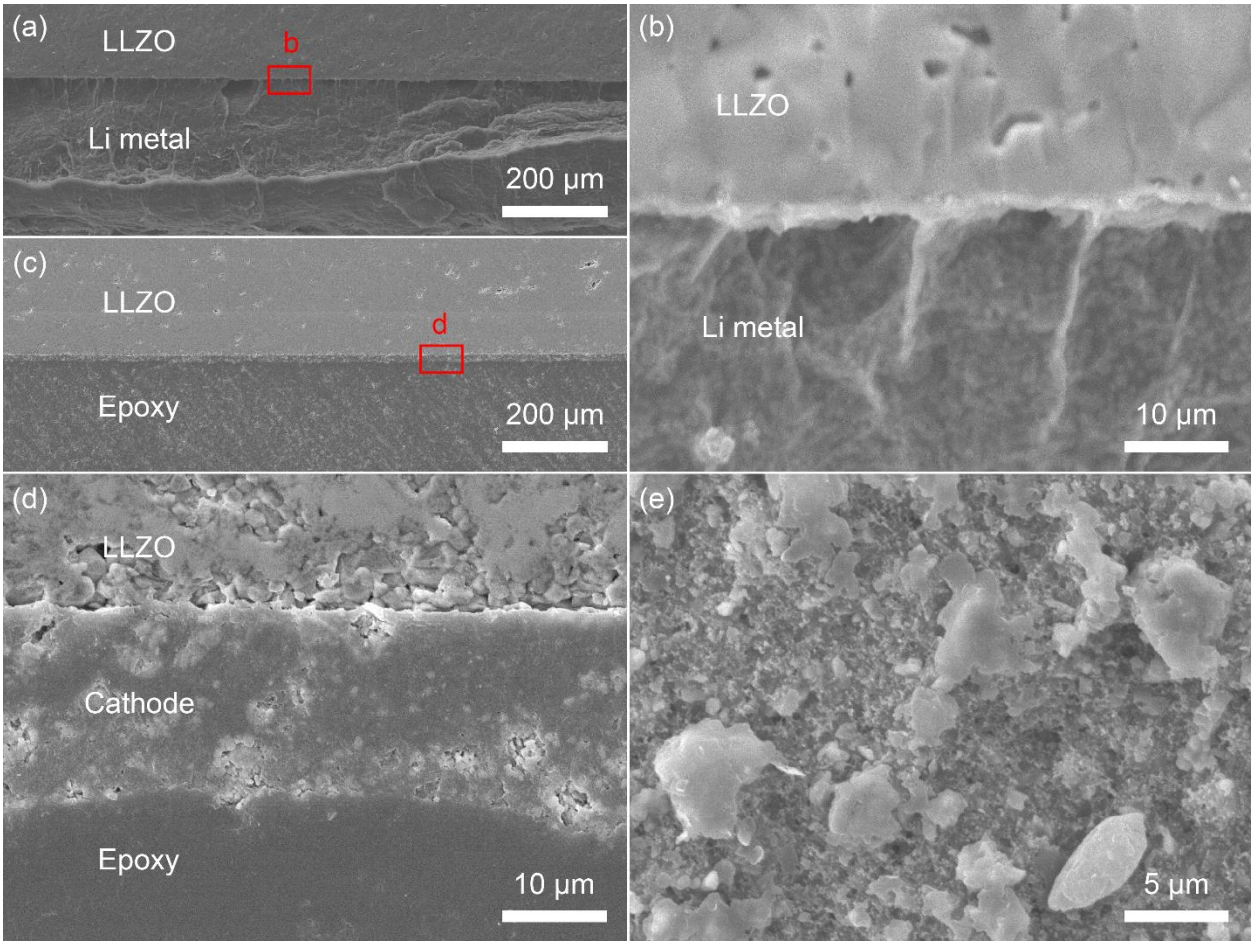

Figure 4. Full cell microstructure. (a) (b) LLZO and Li metal anode interface; (c) (d) LLZO and NMC cathode interface; (e) NMC cathode surface.

3.3 Full cell performance

Full cells containing a cathode with 8.5% LiTFSI and dried at 75 °C for 7 min were cycled at various C-rates at 25 °C (Figure 5). The discharge capacity is 170, 160 and 142 mAh g^{-1} when cycled at 0.1, 0.2 and 0.5 C, respectively. This is comparable with hybrid LLZO cells containing liquid electrolyte in the cathode (Figure S9b). The corresponding energy

density is 399 Wh/kg at 0.1 C, 376 Wh/kg at 0.2 C and 334 Wh/kg at 0.5 C, considering a nominal voltage of 3.75 V for NMC111. Coulombic efficiency at different C-rates is close to 100% after a few initial cycles. The fading is partially attributed to the interfacial resistance growing during cycling, see the inset in Figure 5d. The discharge capacity retention is 68.2% at 0.1 C after 50 cycles, 67.3% at 0.2 C after 60 cycles, and 60.5% at 0.5 C after 125 cycles. For direct comparison, the capacity retention after the first 50 cycles is 68.2% at 0.1 C, 74.3% at 0.2 C, and at 81.8% at 0.5 C. The capacity fades less on a per-cycle basis when cycled at higher C-rates. The time-based discharge capacity fading rate is 4.4%/100 h, 8.1%/100 h and 13.5%/100 h at 0.1 C, 0.2 C and 0.5 C, respectively, shown in Figure S7. For the cell cycled at 0.5 C, the interfacial resistance at low frequency increases more than 5 times, from ~170 to ~1040 Ω cm^2 after 125 cycles. In contrast, the high frequency semicircles assigned to the bulk and grain boundary resistances of the LLZO electrolyte are stable. Possible degradation modes include mechanical failure of the cathode/catholyte upon cycling, NMP migration or evaporation, and side reactions among various materials in the cathode and LLZO. Determining the underlying mechanism of capacity fade is the subject of future work.

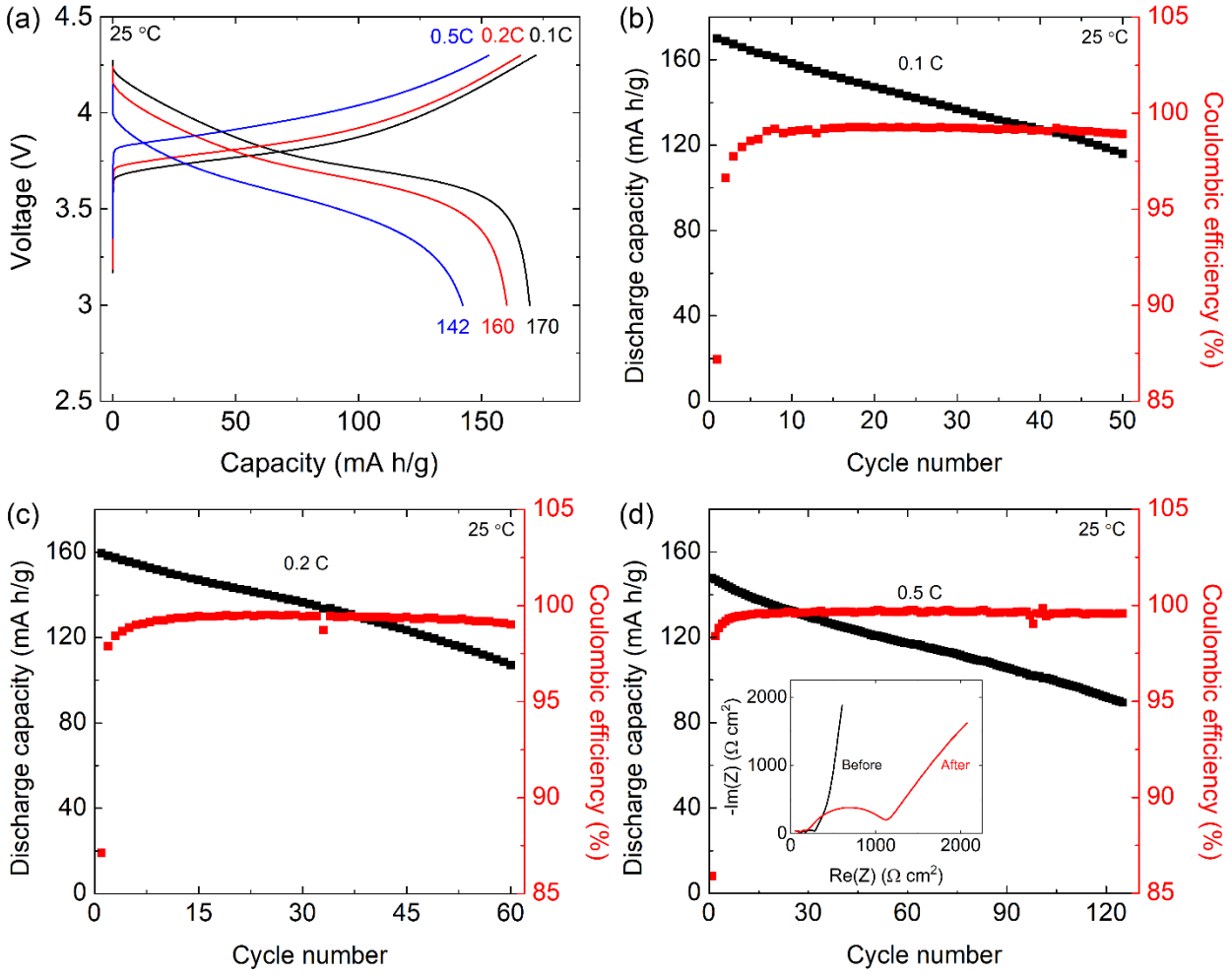

Figure 5. Full cell performance at 25 °C. (a) Charge/discharge curves at 0.1 C, 0.2 C, and 0.5 C; Discharge capacity and coulombic efficiency at (b) 0.1 C, (c) 0.2 C and (d) 0.5 C versus cycle number; The inset in (c) shows EIS of the full cell before (black) and after (red) cycling at 0.5 C.

Low temperature performance is also important for batteries. Cells with residual NMP were also tested at 0 and -10 °C, Figure 6. At 0 °C, the total initial resistance is ~1500 Ω cm^2 and the discharge capacity is 156 mAh g^{-1} at 0.05 C, 147 mAh g^{-1} at 0.1 C, 135 mAh g^{-1} at 0.2 C and 107 mAh g^{-1} at 0.5 C. The cell can still cycle at 0.5 C rate at 0 °C. At -

10 °C, the total initial resistance increases to ~8000 Ω cm^2 and the discharge capacity is 117 mAh g^{-1} at 0.1 C. A typical charge-discharge curve is shown in Figure 6c. The cell shows no degradation in the first 50 cycles but starts degrading after that. The total capacity retention is more than 70% after 100 cycles, a lower fade rate than at 25 °C. EIS before and after 100 cycles at 0.1 C and -10 °C shows the interfacial resistance on the cathode side is tripled, compared to a five-fold increase observed above at 25 °C.

According to the cell performance at high and low temperatures, the discharge capacity of the cells with NMP residue fades faster at higher temperatures. It can be ascribed to the extrinsic degradation-the NMP residue evaporation, leading to a higher interfacial resistance at the cathode side. Moreover, the intrinsic degradation also leads to the cell capacity fading even at -10 °C after ~50 cycles intrinsic. The intrinsic degradation could attribute to the formation of voids on the anode interface and chemomechanical degradation on the cathode interface, such as interface delamination during cycle.[44-46]

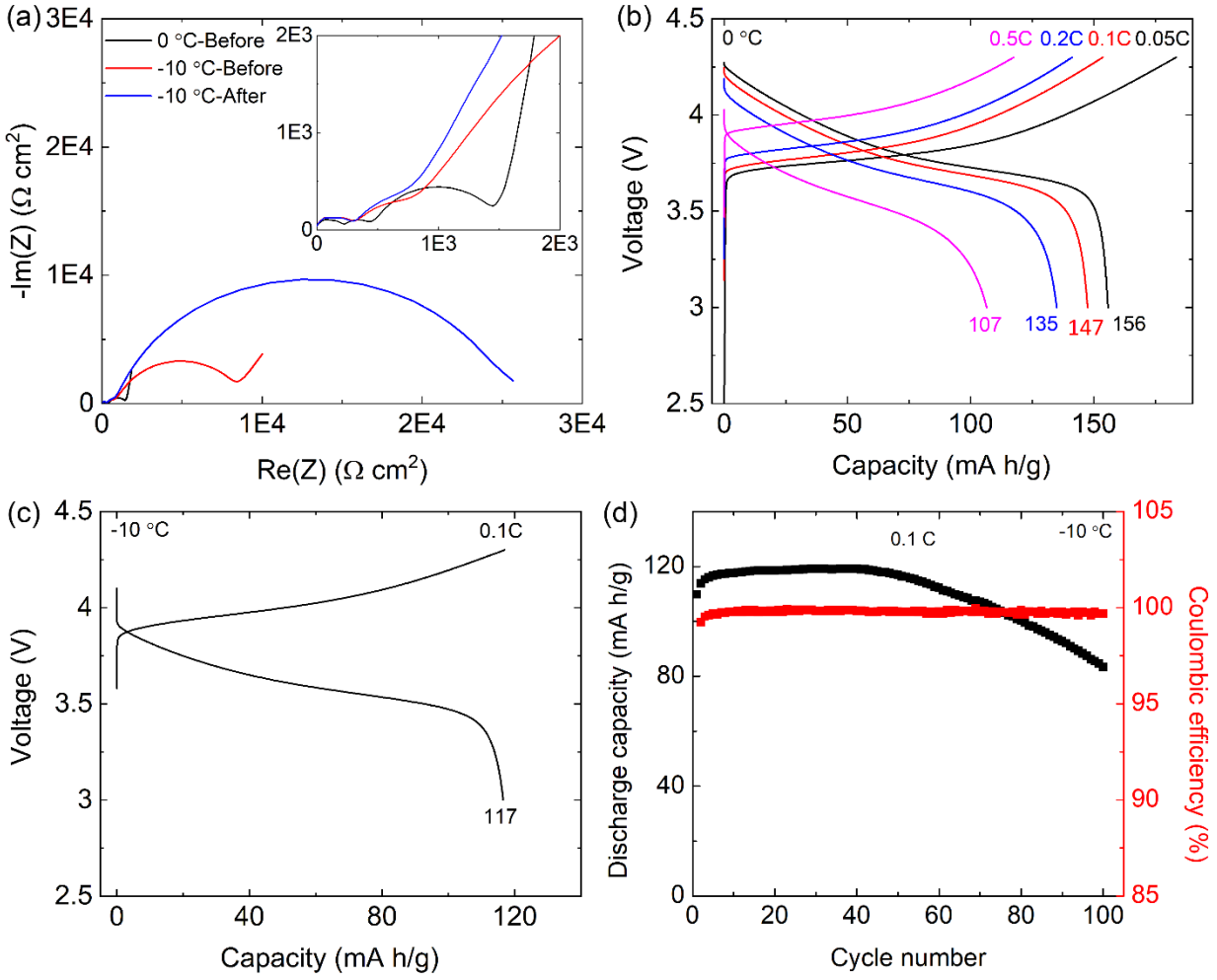

Figure 6. Full cell performance at low temperatures. (a) EIS before and after cycling at 0 °C and -10 °C; (b) Charge/discharge curves at 0 °C with rates of 0.1 C, 0.2 C, 0.5 C, and 1 C; (c) Charge/discharge curves at -10 °C with rate of 0.1 C; (d) Discharge capacity and coulombic efficiency versus cycle number at -10 °C.

The cell performance at high temperature (60 °C) is shown in Figure S8. Very low initial resistance (<50 Ω cm^2) is obtained. However, the discharge capacity is even lower than at the low temperatures. The first charge capacity at 0.1 C is as high as 193 mAh g^{-1}, very

close to the theoretical capacity (200 mAh g^{-1}), but the first discharge capacity is only 154 mAh g^{-1}, lower than at 25 °C. This may be due to the NMP residue evaporating at 60 °C due to the higher vapor pressure (3.413 mmHg at 60 °C vs. 0.347 mmHg at 25 °C), leading to more than 200 times higher interfacial resistance after cycling (from 12 to 2690 Ω cm^2).

As a comparison, hybrid cells were tested with liquid electrolyte added after more thorough drying of the NMP (Figure S9). A cathode with the same composition as the cells with residual NMP was tape cast on an Al current collector and dried at 100 °C overnight under vacuum. Various amounts of liquid electrolyte (1 M $LiPF_6$ in EC/DMC/DEC) were added as catholyte between the cathode and LLZO electrolyte. When an amount of liquid electrolyte similar to the amount of residual NMP after drying for 7 min (~0.2 μL, ~12 wt.% of the cathode) was added, the resistance is ~56,000 Ω cm^2 because this small amount of liquid electrolyte cannot wet the entire cathode. When 5 times this amount of liquid electrolyte (~1 μL, ~58 wt.% of the cathode) was added, the resistance is ~2,000 Ω cm^2, still higher than the cell with residual NMP. When 20 times this amount of liquid electrolyte (~4 μL, ~230 wt.% of the cathode) was added, the resistance is ~500 Ω cm^2, similar to that for the cell with residual NMP (350 Ω cm^2). This hybrid cell with the smallest resistance was cycled at 0.1 C and 25 °C for 50 cycles and the retention is 75.5%, a little better than the cell with residual NMP (68.2% in 50 cycles). The fading of the hybrid cell is ascribed to the reaction between the garnet electrolyte and $LiPF_6$ liquid catholyte. A solid electrolyte interphase, composed of Li_2CO_3, LiF, Li_2O and organic carbonates, is known to grow at the surface of the ceramic electrolyte.[47, 48]

Although similar performance is obtained for cells with residual NMP or hybrid configuration, a higher volume of flammable-liquid is used in the hybrid cell, leading to more safety concern.

3.4 Catholyte conductivity

PVDF with a Li^+ source acts as a catholyte and binder in the cathode, enhancing mechanical properties and ionic conductivity. Its ionic conductivity is reported to be ~$1x10^{-5}$ S cm^{-1} at room temperature as a polymer electrolyte that was dried at 60 °C for 12 h with dimethylformamide as a solvent.[49] However, the huge interface resistance for the completely dried cell (Figure S4) demonstrates its shortcomings as a catholyte in the ASSB design used here. The sensitivity of the interfacial resistance to LiTFSI loading (Figure 3b) suggests that the cathode performance is limited by catholyte conductivity. To further elucidate the conductivity of the PVDF/LiTFSI composite, a free-standing film was prepared by tape casting as a model for the composite catholyte in the cathode. Completely dried PVDF/LiTFSI is a weak ionic conductor, and its conductivity is significantly enhanced by NMP solvent absorption, Figure 7(a). The film was dried at 50 °C for 12 h, after which 3.1 wt% (by TGA) residual NMP remained, as determined by TGA. The ionic conductivity measured in a glove box is $1.0\pm0.1x10^{-5}$ S cm^{-1}. However, when the film was completely dried at 75 °C for 20 h (no residual NMP by TGA), the ionic conductivity drops two orders of magnitude to $1.5\pm0.7x10^{-7}$ S cm^{-1}, which is three orders of magnitude lower than that of the LLZO electrolyte used in this study and four orders of magnitude lower than that of a typical liquid electrolyte.[50] This behavior is broadly consistent with previous work that identified that solvent swelling in a PVDF membrane

acts as a plasticizer and enables useful ionic conductivity, and that drying at higher temperature reduces the conductivity.[35, 36] After air exposure for 10 min, the conductivity of the dried film increases to $3.0\pm1.3\times10^{-5}$ S cm^{-1}, presumably due to moisture uptake by the hygroscopic LiTFSI. This gives a hint that the catholyte conductivity is sensitive to minor amounts of both NMP and moisture, and cathode performance will be impacted by the drying protocol in terms of both atmosphere and temperature history. Yao[36] and Zhang[37] reported that a small amount of DMF remaining in the PVDF-based electrolytes helps to increase the ionic conductivity. The residual DMF exists in the electrolytes in a bound state not as free solvent. The solvent residue also acts as an electrophilic or nucleophilic agent to stabilize the interface between electrolytes and electrodes. In our experiments, NMP residue and moisture play a similar role.

LSV measurement was performed to show the electrochemical window of the free-standing catholyte. The PVDF/LiTFSI film was dried at 50 °C for 12 h with 3.1% NMP remaining. As shown in Figure 7(b), the anodic current started to increase at 4.7 V. This electrochemical window is broad enough for the NMC111 cathode used in this study.

The electronic conductivity of the catholyte was also measured in a glove box. Figure S10 shows the current densit-time curve of the SS/LLZO/SS cell under DC polarization at 0.5 V. The current first decreases and then stabilizes while applying a constant voltage. Electronic conductivity dominates the steady current as lithium ion-blocking electrodes (SS) were used. The electronic conductivity is 2×10^{-12} S/cm, which is extremely low.

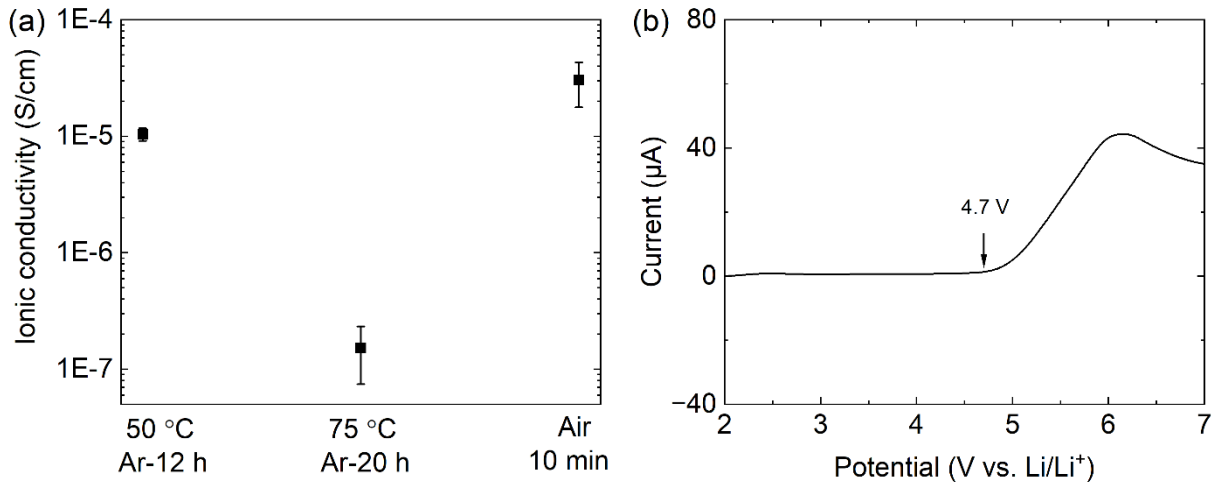

Figure 7. Ionic conductivity and electrochemical stability of the PVDF/LiTFSI film. (a) Ionic conductivity of the 55% PVDF+44% LiTFSI thin films dried at different conditions; (b) LSV curve of the SS/PVDF+LiTFSI/Li cell with PVDF/LiTFSI film dried at 50 °C for 12 h in a glove box.

4. Conclusion

Dense and stable LLZO electrolyte pellets were prepared by sintering in Ar atmosphere, followed by removal of the Li-deficient surface layer by polishing. No dendrite growth was detected for a Li/LLZO/Li symmetric cell cycled at 0.35 mA cm^{-2} over 100 cycles. ASSB cells were prepared with Li metal anode and NMC cathode with PVDF/LiTFSI catholyte. It was found that residual NMP in the cathode has a large impact on cell performance, and incomplete drying therefore reduces the interfacial impedance initially. The amount of residual NMP solvent in the cathode was optimized and the smallest interfacial resistance was obtained with 8.6% NMP. A model study of free-standing PVDF-LiTFSI film suggests that the primary effect of residual NMP is on the catholyte conductivity via

solvent absorption. Also, LiTFSI content was optimized to 8.5%. Full cells were cycled at 60 °C, 25 °C and -10 °C and the highest retention was obtained at -10 °C, showing the temperature-dependence of the capacity fade. Future work should determine the mechanisms of capacity fade. We speculate that incompletely dried cathodes contribute to the widely differing results reported in the literature for ASSBs with polymer catholyte or ion-conducting polymer separator. Further exploration of residual NMP in the cathode could be promising to enhance the electrochemical performance of garnet-based ASSBs.

Author contributions

Fengyu Shen: conceptualization, methodology, data curation, formal analysis, writing-original draft. Robert A. Jonson: conceptualization, writing-review and editing. Michael C. Tucker: conceptualization, writing-review and editing, project administration, funding acquisition. All the authors discussed the results.

Conflict of interest

The authors declare that there is no known competing financial interest.

Acknowledgments

This work was funded by Lawrence Berkeley National Laboratory through the LDRD program and the Vehicle Technologies Office, Office of Energy Efficiency and Renewable Energy, of the U.S. Department of Energy. This research used resources of the Advanced

Light Source (ALS), a DOE Office of Science User Facility under contract no. DE-AC02-05CH11231. The authors thank Dr. Dula Parkinson for help with micro-tomography measurement at Beamline 8.3.2 of ALS. The views and opinions of the authors expressed herein do not necessarily state or reflect those of the United States Government or any agency thereof. Neither the United States Government nor any agency thereof, nor any of their employees, makes any warranty, expressed or implied, or assumes any legal liability or responsibility for the accuracy, completeness, or usefulness of any information, apparatus, product, or process disclosed, or represents that its use would not infringe privately owned rights.

Reference

1. J. B. Goodenough and K. S. Park, *Journal of the American Chemical Society*, 2013, **135**, 1167-1176.
2. A. Masias, J. Marcicki and W. A. Paxton, *Acs Energy Lett*, 2021, **6**, 621-630.
3. Y. Q. Chen, Y. Q. Kang, Y. Zhao, L. Wang, J. L. Liu, Y. X. Li, Z. Liang, X. M. He, X. Li, N. Tavajohi and B. H. Li, *J Energy Chem*, 2021, **59**, 83-99.
4. P. Albertus, S. Babinec, S. Litzelman and A. Newman, *Nature Energy*, 2018, **3**, 16-21.
5. S. X. Xia, X. S. Wu, Z. C. Zhang, Y. Cui and W. Liu, *Chem*, 2019, **5**, 753-785.
6. T. Inoue and K. Mukai, *Acs Appl Mater Inter*, 2017, **9**, 1507-1515.
7. A. Banerjee, X. F. Wang, C. C. Fang, E. A. Wu and Y. S. Meng, *Chem Rev*, 2020, **120**, 6878-6933.
8. K. Takada, *Acta Mater*, 2013, **61**, 759-770.
9. P. Albertus, V. Anandan, C. Ban, N. Balsara, I. Belharouak, J. Buettner-Garrett, Z. Chen, C. Daniel, M. Doeff, N. J. Dudney, B. Dunn, S. J. Harris, S. Herle, E. Herbert, S. Kalnaus, J. A. Libera, D. Lu, S. Martin, B. D. McCloskey, M. T. McDowell, Y. S. Meng, J. Nanda, J. Sakamoto, E. C. Self, S. Tepavcevic, E. Wachsman, C. Wang, A. S. Westover, J. Xiao and T. Yersak, *Acs Energy Lett*, 2021, **6**, 1399-1404.
10. A. Kim, S. Woo, M. Kang, H. Park and B. Kang, *Front Chem*, 2020, **8**.
11. D. Rettenwander, G. Redhammer, F. Preishuber-Pflugl, L. Cheng, L. Miara, R. Wagner, A. Welzl, E. Suard, M. M. Doeff, M. Wilkening, J. Fleig and G. Amthauer, *Chem Mater*, 2016, **28**, 2384-2392.
12. E. Rangasamy, J. Wolfenstine and J. Sakamoto, *Solid State Ionics*, 2012, **206**, 28-32.
13. V. Thangadurai, D. Pinzaru, S. Narayanan and A. K. Baral, *J Phys Chem Lett*, 2015, **6**, 292-299.
14. J. Wang, G. Huang and X. B. Zhang, *Batteries Supercaps*, 2020, **3**, 1006-1015.
15. C. H. Wang, K. Adair and X. L. Sun, *Accounts Mater Res*, 2022, **3**, 21-32.
16. L. M. Riegger, R. Schlem, J. Sann, W. G. Zeier and J. Janek, *Angew Chem Int Edit*, 2021, **60**, 6718-6723.

17. Y. Benabed, M. Rioux, S. Rousselot, G. Hautier and M. Dolle, *Front Energy Res*, 2021, **9**.
18. Z. Z. Tong, S. B. Wang, Y. K. Liao, S. F. Hu and R. S. Liu, *Acs Appl Mater Inter*, 2020, **12**, 47181-47196.
19. X. G. Han, Y. H. Gong, K. Fu, X. F. He, G. T. Hitz, J. Q. Dai, A. Pearse, B. Y. Liu, H. Wang, G. Rublo, Y. F. Mo, V. Thangadurai, E. D. Wachsman and L. B. Hu, *Nat Mater*, 2017, **16**, 572-+.
20. A. Sharafi, E. Kazyak, A. L. Davis, S. H. Yu, T. Thompson, D. J. Siegel, N. P. Dasgupta and J. Sakamoto, *Chem Mater*, 2017, **29**, 7961-7968.
21. G. T. Hitz, D. W. McOwen, L. Zhang, Z. H. Ma, Z. Z. Fu, Y. Wen, Y. H. Gong, J. Q. Dai, T. R. Hamann, L. B. Hu and E. D. Wachsman, *Mater Today*, 2019, **22**, 50-57.
22. F. Y. Shen, M. B. Dixit, W. Zaman, N. Hortance, B. Rogers and K. B. Hatzell, *J Electrochem Soc*, 2019, **166**, A3182-A3188.
23. K. J. Kim and J. L. M. Rupp, *Energ Environ Sci*, 2020, **13**, 4930-4945.
24. F. Y. Shen, R. A. Jonson, D. Y. Parkinson and M. C. Tucker, *J Am Ceram Soc*, 2022, **105**, 90-98.
25. E. Yi, H. Shen, S. Heywood, J. Alvarado, D. Y. Parkinson, G. Y. Chen, S. W. Sofie and M. M. Doeff, *Acs Appl Energ Mater*, 2020, **3**, 170-175.
26. K. Nishio, Y. Gambe, J. Kawaji, A. Unemoto, T. Okumura and I. Honma, *J Electrochem Soc*, 2020, **167**.
27. S. Kim, J.-S. Kim, L. Miara, Y. Wang, S.-K. Jung, S. Y. Park, Z. Song, H. Kim, M. Badding, J. Chang, V. Roev, G. Yoon, R. Kim, J.-H. Kim, K. Yoon, D. Im and K. Kang, *Nat Commun*, 2022, **13**, 1883.
28. W. W. Ping, C. W. Wang, Z. W. Lin, E. Hitz, C. P. Yang, H. Wang and L. B. Hu, *Adv Energy Mater*, 2020, **10**.
29. C. Y. Yan, P. Zhu, H. Jia, Z. Du, J. D. Zhu, R. Orenstein, H. Cheng, N. Q. Wu, M. Dirican and X. W. Zhang, *Energy Storage Mater*, 2020, **26**, 448-456.
30. Y. N. Yang, Y. X. Li, Y. Q. Li and T. Zhang, *Nat Commun*, 2020, **11**.
31. W. J. Lan, H. Y. Fan, V. W. H. Lau, J. L. Zhang, J. Zhang, R. R. Zhao and H. Y. Chen, *Sustain Energ Fuels*, 2020, **4**, 1812-1821.
32. C. Y. Yu, J. Choi, J. Han, E. Lee and J. H. Kim, *J Electrochem Soc*, 2022, **169**.
33. Y. Lu, X. Huang, Y. D. Ruan, Q. S. Wang, R. Kun, J. H. Yang and Z. Y. Wen, *J Mater Chem A*, 2018, **6**, 18853-18858.
34. G. Foran, D. Mankovsky, N. Verdier, D. Lepage, A. Prebe, D. Ayme-Perrot and M. Dolle, *Iscience*, 2020, **23**.
35. C. T. Zhou, S. Bag, B. W. Lv and V. Thangadurai, *J Electrochem Soc*, 2020, **167**.
36. P. C. Yao, B. Zhu, H. W. Zhai, X. B. Liao, Y. X. Zhu, W. H. Xu, Q. Cheng, C. Jayyosi, Z. Li, J. Zhu, K. M. Myers, X. Chen and Y. Yang, *Nano Lett*, 2018, **18**, 6113-6120.
37. X. Zhang, J. Han, X. F. Niu, C. Z. Xin, C. J. Xue, S. Wang, Y. Shen, L. Zhang, L. L. Li and C. W. Nan, *Batteries Supercaps*, 2020, **3**, 876-883.
38. C. H. Liu, R. L. Sacci, R. Sahore, G. M. Veith, N. J. Dudney and X. C. Chen, *J Power Sources*, 2022, **527**.
39. F. Huttner, W. Haselrieder and A. Kwade, *Energy Technol-Ger*, 2020, **8**.
40. R. A. Jonson, E. Yi, F. Y. Shen and M. C. Tucker, *Energ Fuel*, 2021, **35**, 8982-8990.
41. C. L. Tsai, V. Roddatis, C. V. Chandran, Q. L. Ma, S. Uhlenbruck, M. Bram, P. Heitjans and O. Guillon, *Acs Appl Mater Inter*, 2016, **8**, 10617-10626.
42. F. Y. Shen, M. B. Dixit, X. H. Xiao and K. B. Hatzell, *Acs Energy Lett*, 2018, **3**, 1056-1061.
43. S. Afyon, K. V. Kravchyk, S. T. Wang, J. van den Broek, C. Hansel, M. V. Kovalenko and J. L. M. Rupp, *J Mater Chem A*, 2019, **7**, 21299-21308.
44. K. J. Kim, M. Balaish, M. Wadaguchi, L. P. Kong and J. L. M. Rupp, *Adv Energy Mater*, 2021, **11**.
45. X. Zhang, Q. J. Wang, K. L. Harrison, S. A. Roberts and S. J. Harris, *Cell Rep Phys Sci*, 2020, **1**.

46. P. Barai, T. Rojas, B. Narayanan, A. T. Ngo, L. A. Curtiss and V. Srinivasan, *Chem Mater*, 2021, **33**, 5527-5541.
47. J. Y. Liu, X. W. Gao, G. O. Hartley, G. J. Rees, C. Gong, F. H. Richter, J. Janek, Y. Y. Xia, A. W. Robertson, L. R. Johnson and P. G. Bruce, *Joule*, 2020, **4**, 101-108.
48. E. J. Cheng, M. Shoji, T. Abe and K. Kanamura, *Iscience*, 2022, **25**.
49. R. G. Li, D. B. Wu, L. Yu, Y. N. Mei, L. B. Wang, H. Li and X. L. Hu, *Adv Eng Mater*, 2019, **21**.
50. S. S. Zhang, *J Electrochem Soc*, 2013, **160**, A1421-A1424.